Faraday Discussions

Accepted Manuscript

Faraday Discussions

Royal Society of Chemistry

ROYAL SOCIETY OF CHEMISTRY

ROYAL SOCIETY OF CHEMISTRY

www.rsc.org/faraday_d

Reactivity of High Entropy Alloy Nanoparticles under O$_2$ studied by *in situ* Transmission Electron Microscopy

Syrine Krouna[1], Nathaly Ortiz Pena[1], Christian Ricolleau[1], Guillaume Wang[1], Adrien Moncomble[1], Damien Alloyeau[1, *] and Jaysen Nelayah[1, *]

1 Université Paris Cité, CNRS, Laboratoire Matériaux et Phénomènes Quantiques, 75013 Paris, France

* damien.alloyeau@u-paris.fr and jaysen.nelayah@u-paris.fr

Abstract

The gas reactivity of high-entropy nanoalloys (HENAs) is an emerging area of research with significant potential for applications in catalysis, gas sensing, hydrogen storage, and corrosion resistance. Insights into the structure–reactivity relationships that dictate the behavior of HENAs in reactive gas environments are critical for optimizing their performance across these applications. However, understanding the complex structural attributes of HENAs, such as size, shape and structure in response to a gas stimulus, remains challenging because of the limited accessibility to methods capable of probing these attributes under *in situ* or operando conditions. Here, we performed aberration-corrected environmental gas scanning transmission electron microscopy (STEM) observations to investigate the atomic and chemical structures of quinary CoNiCuPtAu HENAs in response to pure oxygen exposure at atmospheric pressure and elevated temperatures. The nanoparticles were fabricated by pulsed laser deposition with a high degree of control over both size and composition. Atomic-scale STEM imaging combined with energy dispersive X-ray (EDX) spectroscopy at the single particle level revealed a complex structural and chemical evolution pathway for CoNiCuPtAu HENAs under oxygen at atmospheric pressure during progressive heating up to 700 °C. Notably, we have identified substantial mass transfers between nanoparticles accompanied by oxygen-induced demixing of components, nanovoid formation and the stabilization of platelet-like nanostructures crystallizing as Co–Ni oxide solid solution.

Faraday Discussions Accepted Manuscript

24 ## 1. Introduction

25 Since the seminal work by Yao et al.[1], mixing multiple metals at the nanoscale to form so-called high-
26 entropy nanoalloys (HENAs) has emerged as a novel strategy for expanding the diversity of metallic
27 nanoparticles (NPs). The combination of atoms with different physicochemical properties, such as atomic
28 radii, cohesive energy, and potential energy, results in a rich variety of atomic and chemical structures.
29 These are typically characterized by a high density of structural defects and significant lattice distortion[2–
30 5]. Consequently, HENAs are proposed to exhibit unusual or enhanced gas reactivity compared to
31 conventional alloys[6,7]. The gas reactivity of HENAs is an emerging field with promising applications in
32 catalysis[8–10], gas sensing[11], hydrogen storage[12] and corrosion resistance[13,14]. To advance both fundamental
33 understanding and technological applications, there is however, an urgent need for *in situ* and operando
34 techniques that can unravel the structure–reactivity relationships governing HENAs' behavior under
35 reactive gas environments. However, studies focusing specifically on the gas-phase interactions of HENAs
36 using these advanced techniques remain limited[15–17]. For example, environmental gas transmission
37 electron microscopy (TEM) has been employed to study both the oxidation of FeCoNiCuPt HENAs in dry
38 air[15] and their reduction under atmospheric hydrogen[16]. These investigations have revealed the complex
39 and dynamic nature of HENAs under gas environments and called for further studies that are capable of
40 probing the structural dynamics of HENAs under relevant gas atmospheres and temperatures, while
41 simultaneously capturing their specific reactivity. Such insights are essential for elucidating how the atomic
42 and chemical structures of HENAs influence their reactivity and how these complex structures, in turn,
43 evolve under realistic reaction conditions. In this context, the present study investigates the reactivity and
44 structural dynamics of CoNiCuPtAu HENAs towards oxygen at atmospheric pressure and high
45 temperatures, using aberration-corrected environmental gas TEM. This approach allows us to capture the
46 structural and chemical dynamics of the nanoalloys under oxidative conditions in real-time and down to
47 the atomic scale, providing new insights into how the stability of HENAs is influenced by reaction
48 conditions.

49 ## 2. Experimental section

50 ### 2.1 Synthesis of HENAs by pulsed laser deposition

51 Pulsed laser deposition has been widely used for the synthesis of bimetallic nanoalloys[18]. This fabrication
52 method is based on the ablation of ultra-pure monometallic targets in a high vacuum chamber using laser
53 irradiation, here a COMPex KrF excimer laser. Alternate ablation of pure metal targets enables the
54 formation of nanoalloys with controlled size and composition on a chosen substrate. The experimental
55 conditions for the fabrication of sub-10 nm CoNiCuPtAu NPs with near equiatomic composition were
56 reported by Barbero et al.[19] In the present study, the same HENA system was studied with the
57 nanoparticles deposited on the SiN membrane of a heating MEMS chip, commercialized by Protochips for
58 *in situ* TEM investigations. During deposition, the substrate temperature was set of 600°C, with a laser
59 frequency of 5 Hz and a total nominal thickness of 4 nm. The deposition rate of each metal was measured
60 prior to synthesis using a quartz crystal microbalance.

61 ### 2.2 *In situ* Scanning Transmission Electron Microscopy

62 *In situ* transmission electron microscopy experiments were carried out on a double aberration-corrected
63 JEOL ARM 200F microscope equipped with a cold field emission gun operating at 200 kV[20]. A Protochips
64 Atmosphere™ high-pressure gas cell (HPGC) was used for *in situ* STEM observations under 1atm O_2 gas
65 pressure. The HPGC comprises two silicon microchips (E-chips) aligned face-to-face in a closed-cell
66 configuration. The smaller E-chip (2 mm × 2 mm × 300 μm) features a 50 nm-thick amorphous SiN window,
67 whereas the larger E-chip (6 mm × 4.5 mm × 300 μm) carries a SiC membrane patterned with six electron-
68 transparent windows (30 nm-thick SiN) for imaging. The CoNiCuPtAu HENAs were synthesized directly on
69 the large E-chip. After assembly of the gas cell, the latter was purged with pure argon (from MESSER; purity
70 ≥ 99.9999%) gas before introducing ultrapure oxygen (from MESSER; purity ≥ 99.9995%) under
71 continuous flow conditions. The sample was heated via resistive heating of the SiC membrane, with a
72 closed-loop temperature control system ensured accurate temperature regulation. *In situ* imaging and
73 video recording were captured in STEM mode using both high-angle annular dark-field (HAADF) and bright-
74 field (BF) detectors, with a 20.5 mrad convergence semi-angle for BF STEM imaging and between 68 and
75 280 mrad for HAADF STEM imaging. Short pixel dwell times (2–3 μs) were used to minimize beam-induced
76 damage. The electron beam was blanked between data capture to further limit electron dose.

3. Result

Using high resolution BF STEM and HAADF STEM imaging combined with spatially-resolved energy dispersive X-ray spectroscopy (EDS), we first investigated the size, structure, and compositional evolution of CoNiCuPtAu NPs under 1 atm oxygen atmosphere during progressive heating up to 700 °C (see supporting Figure S1 for the heating profile). Pure oxygen was introduced at 200 °C, which was the starting temperature for the present studies, knowing that less electron beam–induced contamination occurs at this temperature compared to room temperature. The choice of the temperature range is justified by our previous study on the thermal behaviour of quinary CoNiCuPtAu HENAs in vacuum [21]. In the present study, the same temperature range is applied to enable a direct and meaningful comparison of their thermal stability in vacuum and in an O_2 atmosphere. As shown in Figure 1b, the as-synthesized NPs under Ar, before oxygen exposure, exhibit a size distribution ranging from 2 to 10 nm, with an average diameter of $4.6 \pm 1.4\ nm$. STEM-EDS analysis of single NPs revealed a mean composition of $Co_{15}Ni_{23}Cu_{16}Pt_{29}Au_{17}$ with a standard deviation of 3% (Figure 1c). As shown already[19,21], high-resolution STEM imaging here confirmed that CoNiCuPtAu HENAs crystalize in a face-centered cubic (FCC) solid solution, leading either to FCC single nanocrystals (Figure 1d) or twinned FCC structures (Figure 1e; see also Supporting Information, Figure S2). As discussed in previous work[19,21], CoNiCuPtAu HENAs synthesized via PLD form small monocrystalline NPs, under 3nm, while twinned structures are only observed in bigger NPs.
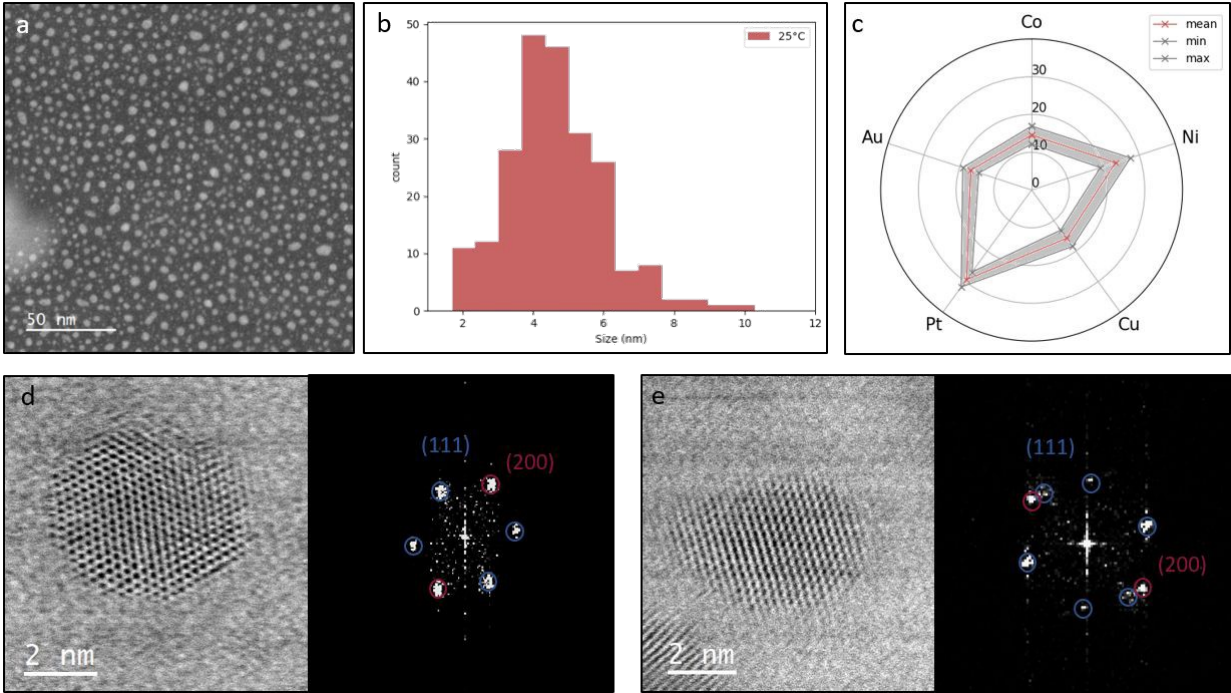
Figure 1. As-prepared CoNiCuPtAu HENAs. a–e) HENA fabricated on the amorphous SiN membrane of a Protochips HPGC a) STEM HAADF image of the HEA NPs. b) Particle size distribution of NPs with a mean diameter around 4 nm. c) Mean composition of NPs represented by the red line and with the shaded grey area indicating the standard deviation. STEM-BF images of a (d) FCC monocrystalline NP observed along its [110] zone axis and e) an FCC twinned NP

Figure 2 presents a temperature series of HAADF-STEM images of the $Co_{15}Ni_{23}Cu_{16}Pt_{29}Au_{17}$ NPs under O_2 between 300 and 700° C. The corresponding NP size distributions, deduced from the analysis of 70 NPs, are represented alongside. We observe that as temperature increases under oxygen, the particle size distribution remains unimodal with the mean NP diameter showing minimal variation throughout the heating cycle. Based solely on this size analysis, it would be tempting to suggest that the CoNiCuPtAu HENAs remains structurally and chemically stable under the applied conditions.

105
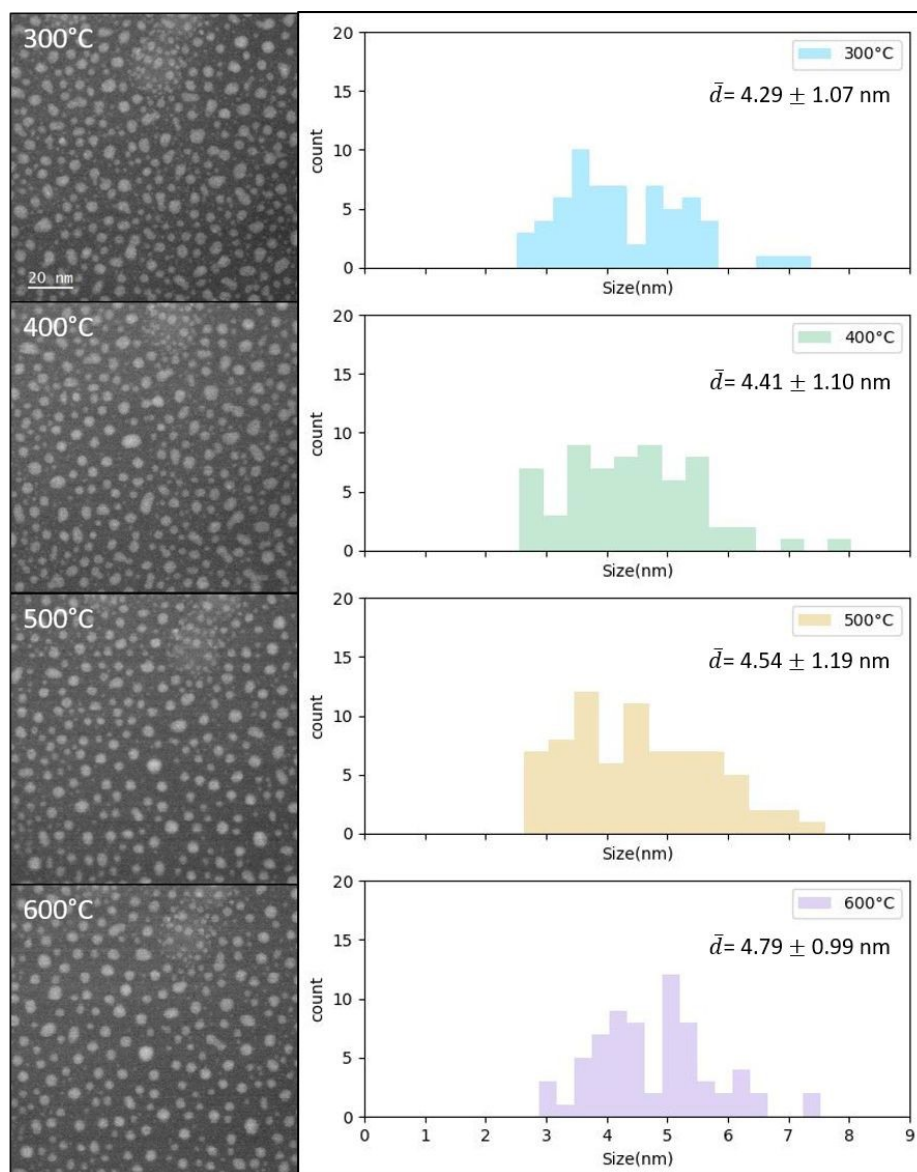
Figure 2. Low resolution STEM image series showing the evolution of HENA under O_2 as a function of the temperature with the corresponding size distribution of NPs. The corresponding mean diameter $\bar{d}$ is indicated in the top-right corner

However, high-resolution STEM analysis (Figure 3), particularly *in situ* STEM video recordings to track particle stability and mobility on the SiN substrate during heating under O_2 (supporting video S1), reveals the activation of the well-known particle growth mechanisms under thermal stimulus: coalescence and Ostwald ripening[18,22,23]. Such growth processes are accompanied by substantial interparticle mass transfer that leads to an increase in the mean particle size.

113

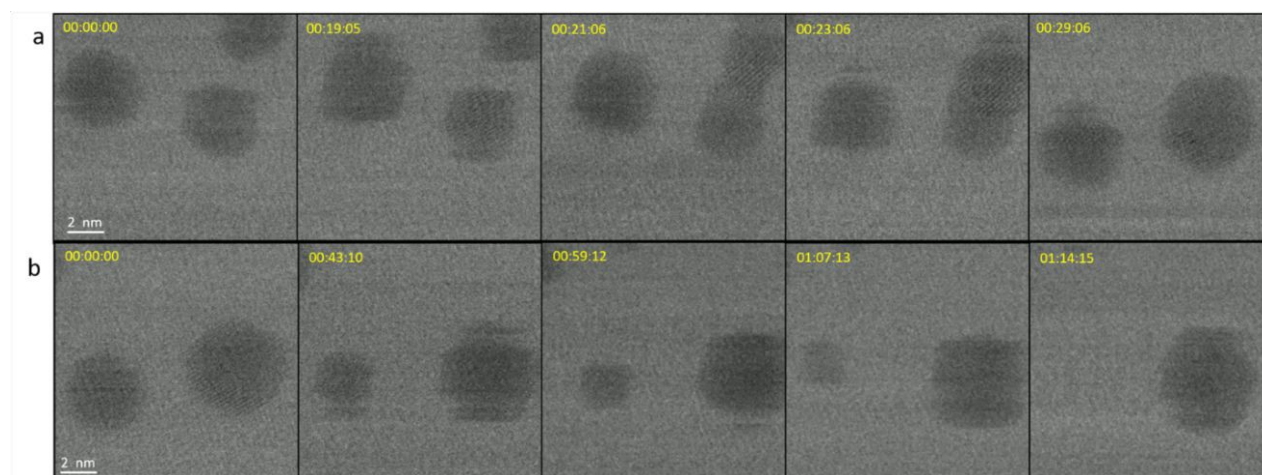*Figure 3. Coarsening events recorded at 700°C involving a) Coalescence and b) Ostwald ripening. The acquisition time is indicated in the top left corner of each image (see associated supporting videos S1)*

116 Yet, this observation is in contraction to the relatively stable particle size distribution revealed by particle

117 size analyses. This apparent contradiction can be explained by an oxygen-induced phenomenon that

118 triggers the demixing of components at high temperatures, followed by phase segregation and subsequent

119 structural rearrangement. In particular, STEM imaging revealed the formation of platelet-like structures

120 which as they grow draw mass from the NPs and offset the expected size increase due to coalescence and

121 Ostwald ripening. The platelets are extremely thin and consequently, exhibit lower Z-contrast than the

122 NPs, which accounts for their visibility only in high-resolution STEM images (Figure 4a and 4b). To identify

123 these structures, we combined high-resolution BF-STEM imaging and compositional analysis via STEM-

124 EDS. Atomic scale analysis of the BF-STEM images revealed two distinct d-spacings of $0.215\ nm$ and

125 $0.241\ nm$, measured within the platelets. In addition, as shown in Figure 4d, STEM-EDS confirmed that

126 these structures contain exclusively cobalt (Co) and nickel (Ni). By comparing our structural and

127 compositional findings with literature data[24], we identify the platelets as a Co–Ni oxide solid solution,

128 $Ni_{1-x}Co_xO$. This compound adopts a NaCl-type crystal structure, where O^{2-} ions occupy the octahedral

129 interstitial sites and Co^{2+}/Ni^{2+} cations randomly populate the FCC lattice positions (see structural model in
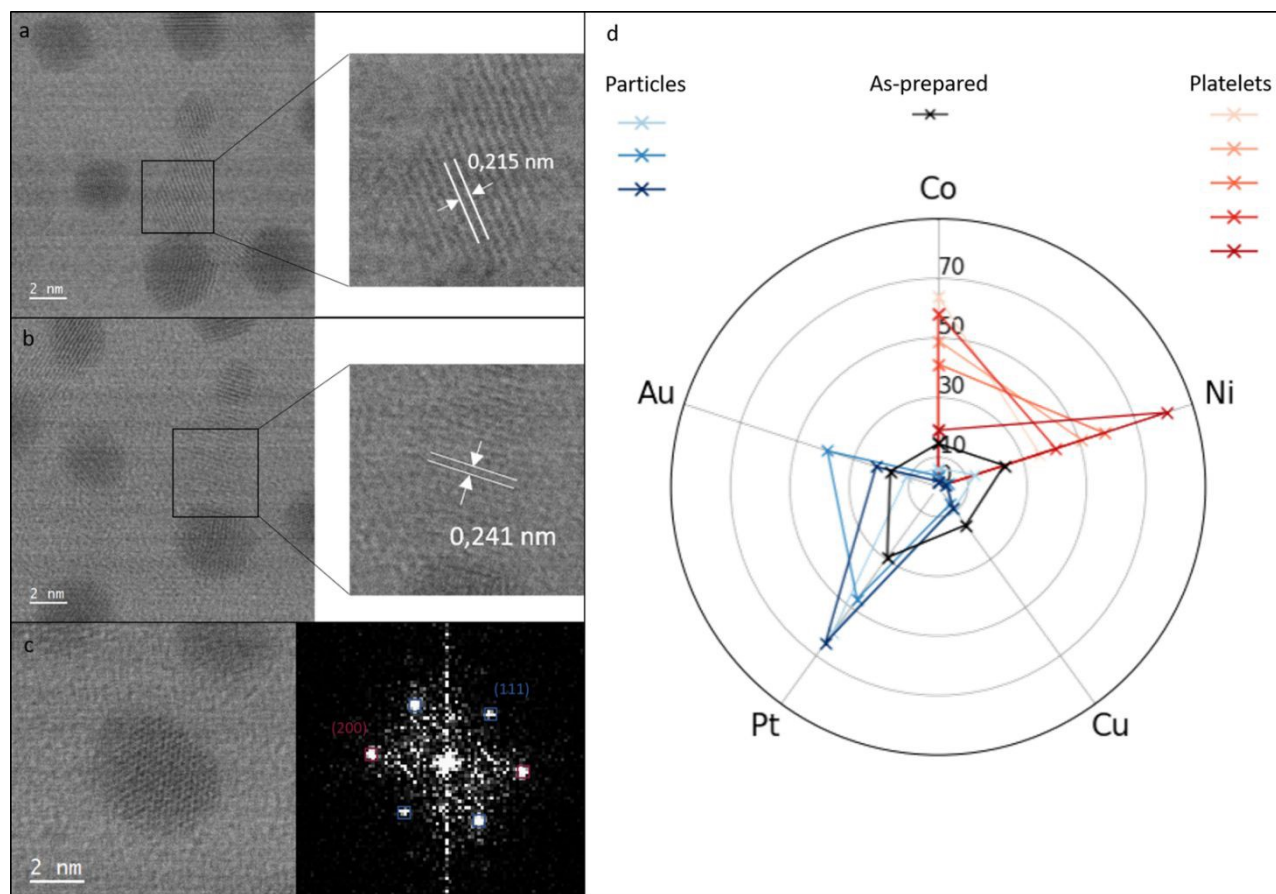
130 supporting information Figure S3).
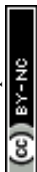
Figure 4. (a) (b) and (c) HR-STEM BF images under O_2 at 200°C after heating up to 700°C presenting structural evolution of CoNiCuPtAu NPs and formation of $Ni_{1-x}Co_xO$ platelets. (a) and (b) High resolution STEM BF images showing platelets with the corresponding d-spacing. (c) High resolution BF STEM image of AuPtCu NP observed along the [110] zone axis. (d) Spider plot showing the composition of the platelets (red lines), the particles (blue lines) and, for reference, the as-prepared composition (black line)

Simultaneously, as shown in Figure 4c, the remaining rounded NPs are well-alloyed, retaining their FCC structure. The compositional spider plot (Figure 4d) highlights the complementarity of the elemental distributions between the platelets and the rounded NPs. These latter are thus mainly composed of Au, Pt and Cu.

Interestingly, high-resolution structural analysis further reveals that the $Ni_{1-x}Co_xO$ platelets grow epitaxially on the rounded NPs. As illustrated in Figure 5 and supporting Figure S4, the platelets commonly share crystallographic orientations with the rounded NPs, primarily along the (111) and (200) planes.
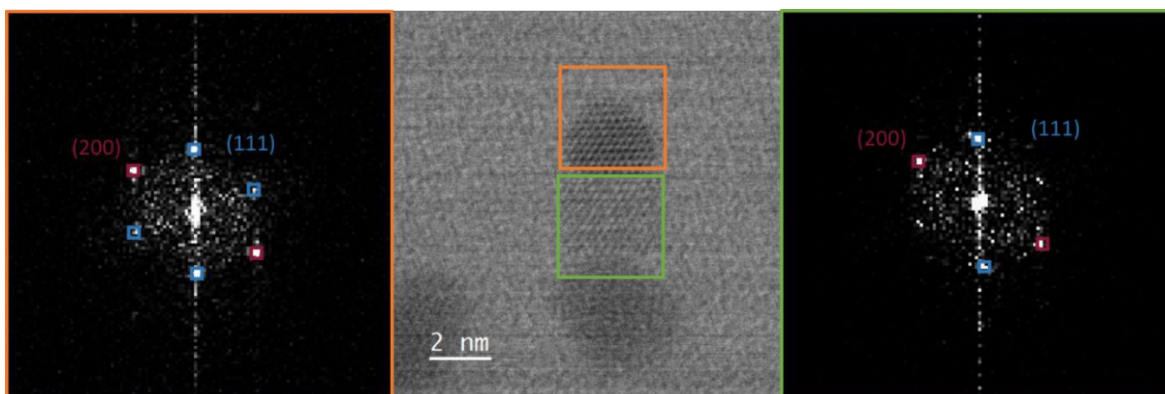
144

Figure 5. In the middle, high resolution STEM images illustrating the epitaxial growth of the $Ni_{1-x}Co_xO$ platelets on the NPs. The FFT on the left and on the right of the HR-STEM image are calculated on the NP (orange frame) and on the platelet (green frame), respectively.

Furthermore, the presence of oxygen triggers the formation of voids within many NPs, as observed by comparing Figures 6a and 6b (supplementary high resolution HAADF STEM images are presented in supporting Figure S5). This phenomenon is attributed to the Kirkendall effect, which arises from the difference in diffusion rates between outward-migrating metal atoms and inward-diffusing oxygen. Notably, this effect, which is well-documented in bulk metallic systems[25,26], monometallic[27–29] and bimetallic NPs[30–35], has not previously been reported in HENAs. These voids are observed exclusively in larger NPs; as shown in Figure 6c, NPs smaller than 4 nm do not exhibit any internal cavities (see supporting video S2). Additionally, very large NPs exhibit multiple voids as illustrated in Figure 6h and 6i. Once formed the voids are highly stable. As shown in the supporting videos S3 and S4, they appear unchanged even when the NPs undergo coalescence. When the NPs are observed along the [110] zone axis, the projected shape of the voids is triangular, characterized by a sharp apex formed between the two edges perpendicular to [111] directions, and a diffuse edge which is perpendicular to [100] (Figure 6d). When the NPs are observed along the [111] zone axis, the projected shape of the voids presents a triangular-like shape with a dark barycenter (figure 6e). To identify the three-dimensional geometry of these voids, their characteristic STEM contrasts along the [110] and [111] zone axes were compared with the STEM contrast for a tetrahedral solid volume bounded by {111} facets in vacuum simulated using kinematic STEM approximations (for more information see the supporting "voids simulation" section and Figure S6) [36]. By inversing the STEM contrast in the simulations, the resulting HAADF images of the solid tetrahedral model are qualitatively similar to those of a tetrahedral void in a bulk material viewed along various zone axes (Figures 6f and 6g). Upon contrast reversal, the simulated STEM contrast closely matches those of the experimentally observed void shapes, providing strong evidence for the tetrahedral 3D shape of the voids.

169
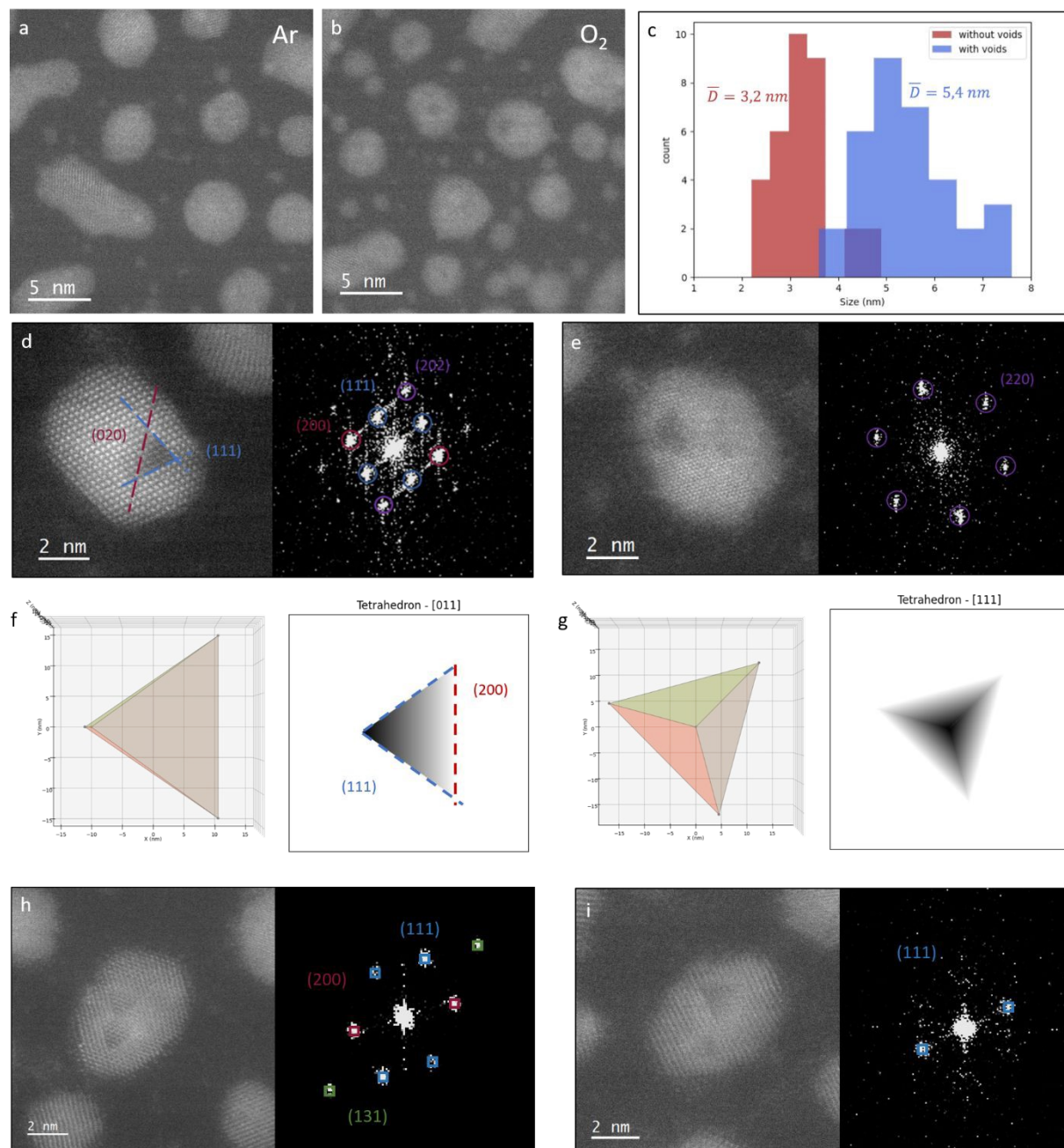
Figure 6. HAADF STEM images showing the voids formed in NP when NPs are exposed to oxygen at 200°C. (a) NPs under Ar before O_2 exposure and (b) under O_2 (c) size distribution of NPs with and without voids. (d) and (e) High resolution HAADF STEM images of NPs presenting a triangular-shaped void along the [110] and [111] zone axes respectively. (f) and (g) Tetrahedral 3D models bounded by {111} facets observed along the [110] and [111] zone axes, respectively. The contrast inversed STEM image of the tetrahedral 3D model calculated by kinematic STEM simulation along the two zone axes are shown alongside. The STEM intensity is inversely proportional to the local thickness upon contrast reversal. (h) and (i) High resolution HAADF STEM images of NPs containing multiple triangular-shaped voids. For stability reason and in order to keep the spatial resolution, high resolution images were acquired under vacuum at room temperature

4. Discussion

179

180   The structural behavior of CoNiCuPtAu HENAs in an oxygen environment is largely governed by the

181   differing reactivities of the constituent elements towards oxygen. Notably, the structural and chemical

182   transformations revealed in the present work differ significantly from those observed when the same HEA

183   NPs undergo thermal treatment in vacuum. In a previous work, where we studied the evolution of the

184   atomic structure of CoNiCuPtAu HENAs between 25 and 700°C using *in situ* thermal TEM and molecular

185   dynamics simulations[21], we highlighted a chemical evolution characterized by the progressive surface

186   segregation and subsequent evaporation of gold and copper atoms from the NPs. This selective elemental

187   segregation was shown to be reinforced by severe shape and surface restructuring upon particle

188   coalescence that occurs at high temperatures (above 400 °C). In particular, experimental observation and

189   numerical simulations revealed that thermally-driven atomic diffusion under vacuum is surprisingly very

190   active in CoNiCuPtAu quinary nanoalloys. In particular, we demonstrated that under vacuum conditions,

191   the structural evolution of CoNiCuPtAu HENAs was governed purely by thermodynamic factors.

192   Surprisingly, their atomic and chemical structures are primarily dictated by surface effects rather than their

193   mixing entropy. The selective segregation of Au and Cu is attributed to their lower surface energies

194   compared to the other constituent elements.

195   In contrast, the presence of oxygen significantly alters this behavior with the oxidation kinetics prevailing

196   over thermodynamic factors and actively directing the structural evolution. As reported by Song et al.[15],

197   based on the formation energy, the tendency for metal oxides formation decreases in the following order

198   for the three non-noble metal considered in this work: Co (1.3 eV/atom), Cu (1.0 eV/atom) and Ni (0.9

199   eV/atom). This hierarchy explains the preferential oxidation of Co and Ni when CoNiCuPtAu HENAs are

200   exposed to oxygen at atmospheric pressure. Interestingly, copper oxides are absent among the oxidation

201   products. This can be attributed to two principal factors: the relatively low diffusion coefficient of copper

202   compared to the ones for cobalt and nickel[15] and the stabilizing effect of gold on copper within the NPs,

203   which likely not only hinders the migration of copper to the surface but also enhances its oxidation

204   resistance. Indeed, it has been already shown [37,38] that the presence of gold enhances the oxidation

205   resistance of copper, particularly in nano-sized objects. It has been proposed that gold reduces the

206   oxidation potential of copper by altering the local electronic structure at the NP surface, decreasing the

207   ability for oxygen to interact with and oxidize copper[37].

208　The formation of voids by Kirkendall effect is well documented and has been previously reported in

209　bulk[25,26]. In nanoparticles as well, oxidation is often accompanied by the Kirkendall effect and void

210　formation. In binary alloyed NPs, incorporating a noble metal can enhance stability towards oxygen and

211　prevent void formation, as observed in systems such as CuPt[39]. In contrast, binary alloyed NPs without this

212　stabilization often exhibit significant void formation during oxidation, as seen in the NiPt system[35]. Various

213　void morphologies have been observed including tetrahedral, octahedral, cubic and hexagonal shapes[25,40].

214　However, to date, tetrahedral-shaped voids have not been reported in multimetallic NPs. The Kirkendall

215　effect arises from the differential diffusion of Co and Ni during the formation of oxide platelets. This leads

216　to the accumulation of vacancies within the NPs. These vacancies tend to locate at the grain

217　boundaries[31,41]. As previously reported[21] and shown in figure 1, CoNiCuPtAu HENAs synthesized via PLD

218　are mostly polycrystalline, with only the smallest NPs (under 3nm) showing monocrystallinity. This

219　structural aspect explains the preferential formation of voids in large NPs. Nevertheless, in very large NPs,

220　we observed the presence of multiple voids. This can be attributed to the low diffusion rate of vacancies,

221　as explained by Railsback et al.[28], which prevents their coalescence into one single void, leading to the

222　stabilization of multiple discrete voids.

223　It is well established that hollow NPs are thermodynamically unstable. In particular, high-temperature

224　annealing typically drives thermal vacancies toward the outer surface, resulting in the transformation of

225　hollow nanocrystals into solid ones through the shrinkage of the nanovoids[42]. In the present study,

226　contrary to expectations, once voids are formed, they remain remarkably stable and persist at elevated

227　temperatures and during coalescence. This suggests that oxygen plays a key role in stabilizing the [111]

228　facets of the voids. Experimental studies carried out by Landeiro Dos Reis et al. revealed that gaseous

229　atmosphere in fact stabilizes voids and vacancies[43]. Atomic-scale simulations were employed to investigate

230　the stability of nanovoids in FCC NPs interacting with hydrogen, considering various particle shape and

231　size. It was shown that hydrogen atoms, which could infiltrate metal lattices and accumulate near voids,

232　play a critical role in pining these nanovoids by stabilizing their size, shape, and growth dynamics compared

233　to hydrogen-free environments. In the present work, the same mechanisms may explain the unexpected

234　stability of the nanovoids observed within CoNiCuPtAu HENAs under oxygen environment, either by

235　stabilizing the inner surfaces through oxide formation or oxygen adsorption. The formation of oxide

236　surfaces or gas adsorption stabilizes low-energy (111) delimiting crystallographic planes, giving rise to the

237　observed tetrahedral shape.

238   Our findings can be contextualized by comparison with the gas-cell TEM study of the oxidation of

239   FeCoNiCuPt HENA performed by Song et al. Although the study was conducted in air rather than pure

240   oxygen, they still observed the formation of voids due to the oxidation of the transition metal Fe, Co, Cu

241   and Ni. However, the study did not include an analysis of the shape and structure of these voids, only the

242   fact that larger NPs did have multiple voids. In addition, the void size appears to scale with NP diameter:

243   in our case, 5 nm NPs exhibited voids smaller than 1 nm, whereas in the study by Song et al., 50 nm NPs

244   contained voids smaller than 10 nm. Furthermore, as discussed previously there is an important

245   compositional effect since the substitution of Fe with Au in our NPs prevented the oxidation of Cu, which

246   contrasts with its oxidation observed in FeCoNiCuPt.

247   In ref [21], we demonstrated that thermal stability of CoNiCuPtAu HENAs under vacuum is governed by

248   temperature and thermodynamic factors such as surface energy. Under O_2, their thermal stability is

249   influenced not only by temperature, but also by the relative affinity of the five constituent elements

250   towards oxygen. These findings, regarding the differing dominant factors influencing the thermal stability

251   in vacuum and in an O_2 environment are likely to be transferable to other HENAs. However, it is likely that

252   the precise behaviour of the HENAs will depend not only on the elements involved but also on their relative

253   concentrations and interaction. Hence, while the general trends of our observations and comparisons may

254   hold, the specific structural and chemical transformations may vary across HENAs.

255   5. Conclusion

256   Despite it being fundamental to real-world gas-related applications, exploration of the behavior of high-

257   entropy nanoalloys in gas environments, particularly under *in situ* or operando conditions, remains limited.

258   In this work, we have addressed this gap in quinary HENAs composed of Co, Ni, Cu, Pt and Au. Notably, we

259   employed aberration-corrected environmental scanning transmission electron microscopy combined with

260   energy-dispersive X-ray spectroscopy to directly observe the atomic and compositional evolution of

261   CoNiCuPtAu HENAs under oxygen exposure at atmospheric pressure and elevated temperatures up to

262   700 °C. This approach allows us to probe their structural and chemical dynamics and interparticle

263   interactions in real time. While particle size distributions appeared stable, *in situ* STEM imaging revealed

264   significant structural dynamics via interparticle mass transfer involving particle coalescence and Ostwald

265   ripening. These processes were accompanied by oxygen-induced demixing, leading to the formation of

266   platelet-like Co–Ni oxide structures. These structures were shown to grow epitaxially on the remaining Au-

267   , Pt-, and Cu-rich ternary NPs. Additionally, we observed, for the first-time void formation within larger

268 NPs, attributed to the Kirkendall effect. This study provides direct atomic-scale evidence of the gas-phase

269 reactivity and structural evolution of CoNiCuPtAu HENAs under oxygen exposure. Contrary to general

270 assumptions of the stability of HEAs, *in situ* environmental STEM observations reveal here that CoNiCuPtAu

271 HENAs undergo pronounced phase segregation and elemental redistribution. It particularly involves the

272 oxidation of less noble components like Co and Ni. Combined with previous knowledge on the thermal

273 stability of CoNiCuPtAu HENAs in vacuum, these findings demonstrate that the thermal stability of HENAs

274 is highly environment-dependent. For tailoring their composition towards more robust catalytic or

275 functional performance under gas environments and at high temperatures, it is thus important that their

276 structure is evaluated under realistic reaction conditions.

277   6. Acknowledgement
278

Faraday Discussions Accepted Manuscript

283   1   Y. Yao, Z. Huang, P. Xie, S. D. Lacey, R. J. Jacob, H. Xie, F. Chen, A. Nie, T. Pu, M. Rehwoldt, D. Yu,
284   M. R. Zachariah, C. Wang, R. Shahbazian-Yassar, J. Li and L. Hu, *Carbothermal shock synthesis of*
285   *high-entropy-alloy nanoparticles*, 2018, vol. 359.

286   2   X. Wang, W. Guo and Y. Fu, *Royal Society of Chemistry*, 2021, preprint, DOI: 10.1039/d0ta09601f.

287   3   L. Yang, R. He, J. Chai, X. Qi, Q. Xue, X. Bi, J. Yu, Z. Sun, L. Xia, K. Wang, N. Kapuria, J. Li, A. Ostovari
288   Moghaddam and A. Cabot, *Advanced Materials*, 2024, **2412337**, 1–53.

289   4   X. Sun and Y. Sun, *Chem Soc Rev*, 2024, **53**, 4400–4433.

290   5   W. Al Zoubi, R. A. K. Putri, M. R. Abukhadra and Y. G. Ko, *Nano Energy*, 2023, **110**, 108362.

291   6   S. K. Dewangan, A. Mangish, S. Kumar, A. Sharma, B. Ahn and V. Kumar, *Engineering Science and*
292   *Technology, an International Journal*, 2022, **35**, 101211.

293   7   Y. Sun and S. Dai, *High-entropy materials for catalysis: A new frontier*, 2021, vol. 7.

294   8   L. Yu, K. Zeng, C. Li, X. Lin, H. Liu, W. Shi, H.-J. J. Qiu, Y. Yuan and Y. Yao, *Carbon Energy*, 2022, **4**,
295   731–761.

296   9   Y. Xin, S. Li, Y. Qian, W. Zhu, H. Yuan, P. Jiang, R. Guo and L. Wang, *ACS Catal*, 2020, **10**, 11280–
297   11306.

298   10   S. Shafeie, S. Guo, Q. Hu, H. Fahlquist, P. Erhart and A. Palmqvist, *J Appl Phys*,
299   DOI:10.1063/1.4935489.

300   11   S. Kumar and M. Kumar, *Transactions of the Indian National Academy of Engineering*, 2024, **9**,
301   679–687.

302   12   F. Marques, M. Balcerzak, F. Winkelmann, G. Zepon and M. Felderhoff, *Energy Environ Sci*, 2021,
303   **14**, 5191–5227.

304   13   H. Xu, J. Zang, Y. Yuan, Y. Zhou, P. Tian and Y. Wang, *J Alloys Compd*, 2019, **811**, 152082.

305   14   X. Yan, W. Yang, Y. Meng, Z. Liao, S. Pang, Q. Wang, P. K. Liaw and T. Zhang, *J Alloys Compd*, 2023,
306   **960**, 170757.

307   15   B. Song, Y. Yang, M. Rabbani, T. T. Yang, K. He, X. Hu, Y. Yuan, P. Ghildiyal, V. P. Dravid, M. R.
308   Zachariah, W. A. Saidi, Y. Liu and R. Shahbazian-Yassar, *ACS Nano*, 2020, **14**, 15131–15143.

309   16   B. Song, Y. Yang, T. T. Yang, K. He, X. Hu, Y. Yuan, V. P. Dravid, M. R. Zachariah, W. A. Saidi, Y. Liu
310   and R. Shahbazian-Yassar, *Nano Lett*, 2021, **21**, 1742–1748.

311   17   Y. Li, C. K. Peng, Y. Sun, L. D. N. Sui, Y. C. Chang, S. Y. Chen, Y. Zhou, Y. G. Lin and J. M. Lee, *Nature*
312   *Communications 2024 15:1*, 2024, **15**, 1–13.

313   18   D. Alloyeau, T. Oikawa, J. Nelayah, G. Wang and C. Ricolleau, *Appl Phys Lett*,
314   DOI:10.1063/1.4754111.

315   19   A. Barbero, C. Moreira Da Silva, N. Ortiz Pena, N. Kefane, A. Jaafar, M. Thorey, H. Bouaia, J.
316   Nelayah, G. Wang, H. Amara, C. Ricolleau, V. Huc and D. Alloyeau, *Faraday Discuss*, 2022, **375**,
317   129–143.

Faraday Discussions Accepted Manuscript

318 20   C. Ricolleau, J. Nelayah, T. Oikawa, Y. Kohno, G. Wang, F. Hue, L. Florea, V. Pierron, D. Alloyeau, C.
319   Ricolleau, J. Nelayah, T. Oikawa, Y. Kohno and N. Braidy, .

320 21   S. Krouna, A. Acheche, G. Wang, N. O. Pena, R. Gatti, C. Ricolleau, H. Amara, J. Nelayah and D.
321   Alloyeau, *Advanced Materials*, 2024, **2414510**, 1–10.

322 22   G. Prévot, N. T. Nguyen, D. Alloyeau, C. Ricolleau and J. Nelayah, *ACS Nano*, 2016, **10**, 4127–4133.

323 23   D. Alloyeau, G. Prévot, Y. Le Bouar, T. Oikawa, C. Langlois, A. Loiseau and C. Ricolleau, *Phys Rev
324   Lett*, DOI:10.1103/PhysRevLett.105.255901.

325 24   S. Kuboon and Y. H. Hu, *Ind Eng Chem Res*, 2011, **50**, 2015–2020.

326 25   A. Meldrum, S. Honda, C. W. White, R. A. Zuhr and L. A. Boatner, *J Mater Res*, 2001, **16**, 2670–
327   2679.

328 26   Y. Yin, R. M. Rioux, C. K. Erdonmez, S. Hughes, G. A. Somorjal and A. P. Alivisatos, *Science (1979)*,
329   2004, **304**, 711–714.

330 27   M. Varón, I. Ojea-Jimenez, J. Arbiol, L. Balcells, B. Martínez and V. F. Puntes, *Nanoscale*, 2013, **5**,
331   2429–2436.

332 28   J. G. Railsback, A. C. Johnston-Peck, J. Wang and J. B. Tracy, *ACS Nano*, 2010, **4**, 1913–1920.

333 29   K. Y. Niu, J. Park, H. Zheng and A. P. Alivisatos, *Nano Lett*, 2013, **13**, 5715–5719.

334 30   W. Wu and M. M. Maye, *Small*, 2014, **10**, 271–276.

335 31   J. Huang, Y. Yan, X. Li, X. Qiao, X. Wu, J. Li, R. Shen, D. Yang and H. Zhang, *Nano Res*, 2020, **13**,
336   2641–2649.

337 32   C. M. Wang, A. Genc, H. Cheng, L. Pullan, D. R. Baer and S. M. Bruemmer, *Sci Rep*, 2015, **4**, 1–6.

338 33   W. Xia, Y. Yang, Q. Meng, Z. Deng, M. Gong, J. Wang, D. Wang, Y. Zhu, L. Sun, F. Xu, J. Li and H. L.
339   Xin, *ACS Nano*, 2018, **12**, 7866–7874.

340 34   L. Han, Q. Meng, D. Wang, Y. Zhu, J. Wang, X. Du, E. A. Stach and H. L. Xin, *Nat Commun*, 2016, **7**,
341   1–9.

342 35   S. F. Tan, S. W. Chee, Z. Baraissov, H. Jin, T. L. Tan and U. Mirsaidov, *Adv Funct Mater*, 2019, **29**, 1–
343   10.

344 36   A. Moncomble, D. Alloyeau, M. Moreaud, A. Khelfa, G. Wang, N. Ortiz-Peña, H. Amara, R. Gatti, R.
345   Moreau, C. Ricolleau and J. Nelayah, *Ultramicroscopy*, 2025, **271**, 114121.

346 37   X. Liu, J. Ruiz and D. Astruc, *Chemical Communications*, 2017, **53**, 11134–11137.

347 38   A. Wilson, R. Bernard, Y. Borensztein, B. Croset, H. Cruguel, A. Vlad, A. Coati, Y. Garreau and G.
348   Prévot, *Journal of Physical Chemistry Letters*, 2015, **6**, 2050–2055.

349 39   A. C. Foucher, S. Yang, D. J. Rosen, R. Huang, J. B. Pyo, O. Kwon, C. J. Owen, D. F. Sanchez, I. I.
350   Sadykov, D. Grolimund, B. Kozinsky, A. I. Frenkel, R. J. Gorte, C. B. Murray and E. A. Stach, *J Am
351   Chem Soc*, 2023, **145**, 5410–5421.

352   40   S. Kondo, Y. Katoh and L. L. Snead, *Appl Phys Lett*, DOI:10.1063/1.3005650.

353   41   A. A. El Mel, M. Buffière, P. Y. Tessier, S. Konstantinidis, W. Xu, K. Du, I. Wathuthanthri, C. H. Choi,
354   C. Bittencourt and R. Snyders, *Small*, 2013, **9**, 2838–2843.

355   42   L. Dubau, J. Nelayah, S. Moldovan, O. Ersen, P. Bordet, J. Drnec, T. Asset, R. Chattot and F.
356   Maillard, *ACS Catal*, 2016, **6**, 4673–4684.

357   43   M. Landeiro Dos Reis, Y. Ferro, A. Oudriss and X. Feaugas, *Acta Mater*, 2024, **281**, 120400.

358

Data Availability

The data supporting this article have been included as part of the Main article and the Supplementary Information